China Geology 7 (2024) 171−187

China Geology

Journal homepage: http://chinageology.cgs.cn
https://www.sciencedirect.com/journal/china-geology

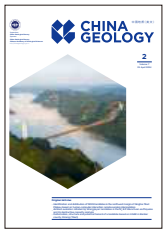

Identification and distribution of 13003 landslides in the northwest margin of Qinghai-Tibet Plateau based on human-computer interaction remote sensing interpretation

Wei Wang[a, b], Yuan-dong Huang[a, c], Chong Xu[a, b,*], Xiao-yi Shao[a, b], Lei Li[a], Li-ye Feng[d], Hui-ran Gao[a, b], Yu-long Cui[e], Shuai Wu[e], Zhi-qiang Yang[a, b], Kai Ma[f]

[a] *National Institute of Natural Hazards, Ministry of Emergency Management of China, Beijing* 100085, *China*
[b] *Key Laboratory of Compound and Chained Natural Hazards Dynamics, Ministry of Emergency Management of China, Beijing* 100085, *China*
[c] *School of Emergency Management Science and Engineering, University of Chinese Academy of Sciences, Beijing* 100049, *China*
[d] *School of Soil and Water Conservation, Beijing Forestry University, Beijing* 100083, *China*
[e] *School of Civil Engineering and Architecture, Anhui University of Science and Technology, Huainan* 232001, *China*
[f] *No.3 Bureau of China Metallurgical Geology Bureau, Taiyuan* 030031, *China*

ARTICLE INFO

Article history:
Received 15 December 2023
Received in revised form 28 January 2024
Accepted 18 February 2024
Available online 12 April 2024

Keywords:
Landslides
Human-computer interaction interpretation
Landslide database
Spatial distribution
Earthquake
Rainfall
Human engineering activity
Qinghai-Tibet Plateau
Geological hazards survey engineering

ABSTRACT

The periphery of the Qinghai-Tibet Plateau is renowned for its susceptibility to landslides. However, the northwestern margin of this region, characterised by limited human activities and challenging transportation, remains insufficiently explored concerning landslide occurrence and dispersion. With the planning and construction of the Xinjiang-Tibet Railway, a comprehensive investigation into disastrous landslides in this area is essential for effective disaster preparedness and mitigation strategies. By using the human-computer interaction interpretation approach, the authors established a landslide database encompassing 13003 landslides, collectively spanning an area of 3351.24 km^2 (36°N–40°N, 73°E–78°E). The database incorporates diverse topographical and environmental parameters, including regional elevation, slope angle, slope aspect, distance to faults, distance to roads, distance to rivers, annual precipitation, and stratum. The statistical characteristics of number and area of landslides, landslide number density (LND), and landslide area percentage (LAP) are analyzed. The authors found that a predominant concentration of landslide origins within high slope angle regions, with the highest incidence observed in intervals characterised by average slopes of 20° to 30°, maximum slope angle above 80°, along with orientations towards the north (N), northeast (NE), and southwest (SW). Additionally, elevations above 4.5 km, distance to rivers below 1 km, rainfall between 20–30 mm and 30–40 mm emerge as particularly susceptible to landslide development. The study area's geological composition primarily comprises Mesozoic and Upper Paleozoic outcrops. Both fault and human engineering activities have different degrees of influence on landslide development. Furthermore, the significance of the landslide database, the relationship between landslide distribution and environmental factors, and the geometric and morphological characteristics of landslides are discussed. The landslide H/L ratios in the study area are mainly concentrated between 0.4 and 0.64. It means the landslides mobility in the region is relatively low, and the authors speculate that landslides in this region more possibly triggered by earthquakes or located in meizoseismal area.

1. Introduction

Landslide hazards threaten both society and human lives, often resulting in substantial damage and casualties (Xu C et al., 2015). Regional landslide databases are essential in understanding the regularities of landslide distributions (Guzzetti F et al., 2012; Xu C et al., 2014a; Xu C, 2015; Roback K et al., 2018), geomorphic evolution (Borgatti L and Soldati M, 2010; Parker RN et al., 2011) and hazard assessment (Xu C et al., 2012a; Ma S and Xu C, 2019; Shao X et al., 2019). In addition to such transient landslides, the study of ancient landslides, originating from protracted slope

First author: *E-mail address*: weiwang@ninhm.ac.cn (Wei Wang).
* Corresponding author: *E-mail address*: xc11111111@126.com (Chong Xu).

Literary editor: Li-qiong Jia
doi:10.31035/cg2023140
2096-5192/© 2024 China Geology Editorial Office.

movements and climatic-tectonic interplays, has become integral to geohazard preparedness (Rao G et al., 2017; Zhang Y et al., 2018). For instance, Nilsen TH et al. (1975) researched the influence of rainfall and ancient landslide deposits on recent landslides in urban areas of Contra Costa County, California. Dewitte O et al. (2006) selected a study area comprised of 13 ancient landslides located in the Flemish Ardennes (West Belgium) and predicted the hazard related to scarp retreat. Pánek T et al. (2008) investigated the structure and chronology of the giant ancient landslide in the Alma water gap (Crimean Mountains, Ukraine). Georgi F and Krastanov M (2015) analysed and evaluated the possibilities for construction on the ancient landslide, which is located on the Black Sea coast in southeastern peripheral part of Dobrudja plateau, Bulgaria. Kohno M and Yuki H (2023) drew the landslide susceptibility mapping along the whole slope of the Japanese archipelago based on the ancient landslide topography. Chen Y et al. (2022) analysed the morphological scale and spatial distribution characteristics of 1158 ancient landslides near the Shuicheng landslide. Similarly, Cui Y et al. (2023) investigated the spatial distribution features of ancient landslides in the Western Himalayan tectonic knob region, offering a comprehensive evaluation of regional landslide hazards. In the context of Hualong County, Huang Y et al. (2023) meticulously constructed an inventory of large landslides and ancient landslides, employing visual interpretation of remote sensing imagery coupled with on-site survey validation. Examining the Xuecheng area in Li County, Sichuan Province, Ma S and Xu C (2021) delved into a two-year study of deformation dynamics pertaining to a substantial ancient landslide (approximately 35×10^6 m^3 in volume), dissecting potential triggers and the revival mechanism of this ancient landslide mass. Furthermore, Shao X et al. (2022) and Chen Z et al. (2023) established a comprehensive database cataloguing coseismic landslides resulting from the M_S 5.8, M_S 6.0, and M_S 5.2 earthquake swarms in Markang, Sichuan, China.

The periphery of the Qinghai-Tibet Plateau is characterised by a high number of natural disasters with extensive reach and high economic losses (Cui P et al., 2015; Qi W et al., 2021; Zhao B et al., 2023). Scholars have conducted in-depth studies on the active tectonics in the region (Reznichenko NV et al., 2017; Chevalier ML, 2019). Scholars have also studied the characteristics and ages of large landslides in the northeastern part of the region, and found that large landslides was directly proportional to the intensity of precipitation and monsoon activity (Yuan Z, 2012; Yuan Z et al., 2013). In addition, some researches on monomer landslide have been carried out. For instance, from the perspective of the occurrence time of the landslide and geomorphologic feature of the deposits, Zhu Y et al. (2019) proposed that the landslide was not caused by glacier activity and freeze-thaw events, and thus, must have been triggered by an earthquake. The long runout of the Taheman landslide is mainly caused by its large volume and the interaction of the slide mass with moraines. Based on the geological phenomena in the field and the research results of predecessors, Wang J (2020) determined that the momentum transmission mechanism is the main mechanism when Taheman landslide slides in the slip source area, and the particle debris fluidization drag reduction is the dynamic mechanism of Taheman landslide long-distance movement. Shi A et al. (2023) analyzed the geological background of the Lymek landslide and the material composition of the bedrock in the source area, determined the co-seismic initiation mechanism of the Lymek landslide. And reconstructed the initial topography of the source area and the accumulation area. The Lymek landslide has been identified as the largest high-speed, long-distance landslide known to Chinese mainland.

There are some special studies on large monomer landslide in the study area. However, a comprehensive landslide database for the northwest Qinghai-Tibet Plateau margin is still missing. This gap hampers the researchers' grasp of regional landslide extent and distribution (Shao X et al., 2020). With the planning and construction of several major projects, such as the "Xinjiang-Tibet Railway", the importance of this study area has become more prominent. The region is characterised by widespread geological hazards, encompassing landslides of varying magnitudes and fault systems. These challenges pose considerable threats to the railway's secure operation, imperilling transportation safety and diminishing its efficiency as a crucial mode of transportation (Ma D et al., 2003; Wang P, 2020). Therefore, investigating the underlying causes and projecting the trajectory of landslide risks along railway routes becomes paramount. Based on previous work (Wang W et al., 2021), the authors build a more detailed and complete landslide database, and analyzed the characteristics of these landslides. This study is important for understanding the evolution of this region's landforms and seismic activity. Furthermore, it aids in predicting landslides and managing disasters here. Additionally, it serves as a reference for studying similar landslides elsewhere.

2. Geological setting

The study area is on the western edge of China, bordering Kyrgyzstan, Tajikistan, Afghanistan and Pakistan. Geographically, it occupies the northwestern corner of the Qinghai-Tibet Plateau, with coordinates spanning from 36°N to 40°N and 73°E to 78°E (Fig. 1). For the study area, the Pamir Plateau occupies the right side, while Tarim Basin is found on the left side. In terms of regional tectonics, some large tectonic zones are widely distributed, concentrated in the eastern Pamir Plateau. Among these, the most prominent fault zone is the Gonggeer/Brunkou extensional fault zone, oriented NW–SE and extending over approximately 250 km. This zone exhibits the highest tectonic stress levels and showcases the swiftest rates of crustal denudation and uplift across the Qinghai-Tibet Plateau (Brunel M et al., 1994; Schurr B et al., 2014). Additionally, significant large-scale tectonic features encompass the Main Pamir Reverse Fault Zone and the Muji Fault (Li W, 2013; Deng J et al., 2020). The distribution of lake and river systems in the study area is

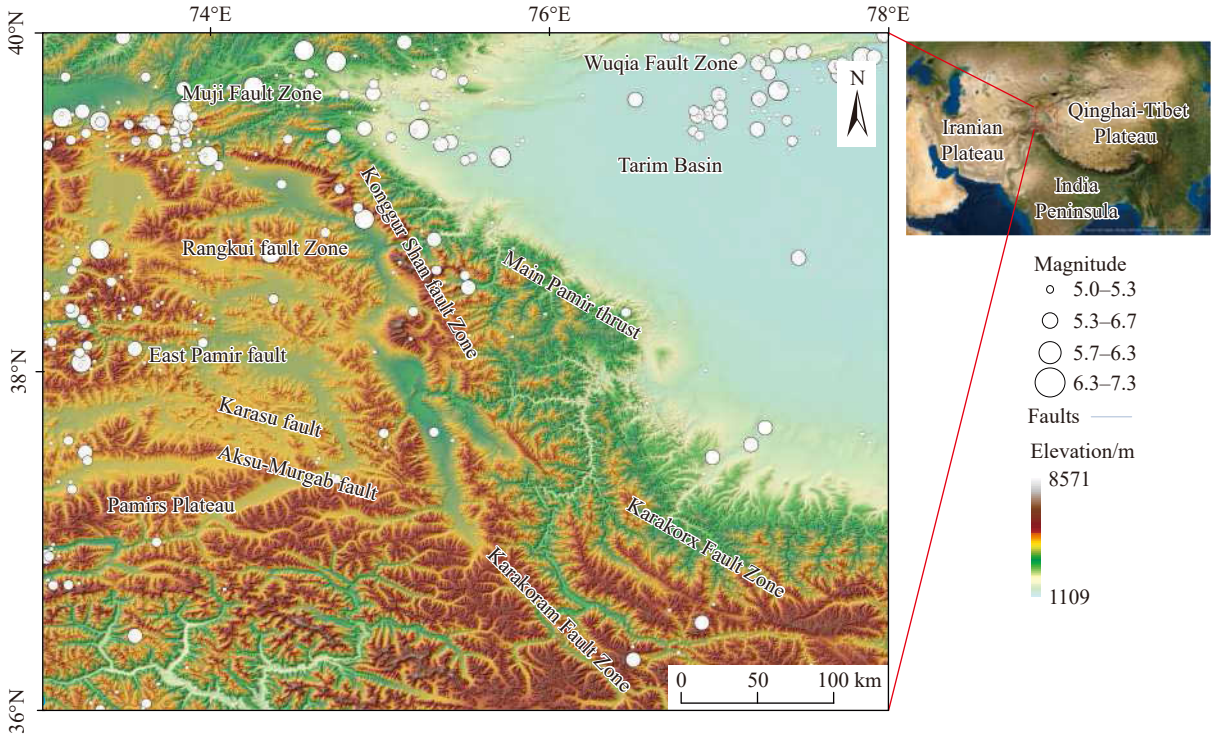

Fig. 1. Tectonic background of the study area.

dense, including the famous Kanshiva River and Karakul Lake. Seismic activities of the study area are concentrated around the Muji fault and the Wuqia fault zone. A total of 324 earthquakes with magnitudes surpassing 5 have occurred, and the maximum magnitude is M_S 7.3 in 1974 near Eshme, Kyrgyzstan, situated 134 km east of Kyzyl-Eshme (data from the U.S. Geological Survey, https://earthquake.usgs.gov/earthquakes/search/).

Fig. 2 shows the geological map of the study area data from the China Geological Survey (1∶4000000). The stratum of the study area is complex, with the earliest age being the Archean strata. Based on the area covered, the major lithologies in the study area include Cenozoic sedimentary rocks and Palaeozoic gneisses and schists. The study area has a wide range of elevation and temperature variations. The maximum monthly ground temperature in the regions around Tarim Basin has over 30°C (Fu W et al., 2003), and some areas are very cold and there are a lot of Quaternary glaciers (Seong YB et al., 2009).

3. Data and methods

3.1. Data

DEM data, geological maps, remote sensing images and road network are employed in this study. A large amount of important environmental information was extracted into the database (Fig. 3). Various databases were established for factors including regional elevation, slope angle, slope aspect, distance to faults (the faults mentioned in this study are all active faults), distance to roads, distance to rivers, average precipitation, and stratum. The data sources are shown in Table 1.

The landslide dataset established in this study spans a considerable timeframe. Variability in temporal scales between these records and collected environmental factors introduces discrepancies. Nevertheless, the underlying geographical factors, such as topography, hydrology, and geology, have exhibited relative stability over extended periods, minimizing the temporal incongruities' impact on this study's characterisation. The interannual variability in rainfall was likely to be high. To mitigate this, this study adopted mean annual rainfall for analysing the connection between rainfall and landslides, thereby mitigating the influence of temporal rainfall variations.

3.2. Methods

The authors employed a human-computer interaction interpretation approach to identify recognizable landslides, utilising the Google Earth platform with images offering a maximum resolution of 0.5 m. Then, the authors conducted statistical analysis on the number of landslides, landslide area, landslide number density (LND), and landslide area percentage (LAP) in the factor intervals. These indicators formed the basis for assessing landslide development within these intervals. The recognizable landslides referred to in this study included ancient landslides and areas with significant deformation, and areas with no significant geomorphologic changes were not identified. Key indicators for interpretation primarily hinge on morphological characteristics of these landslides, including the following: (1) The back wall of the landslide often shows a lap-chair shape with curved ridgelines; (2) middle and rear parts of the landslide body may

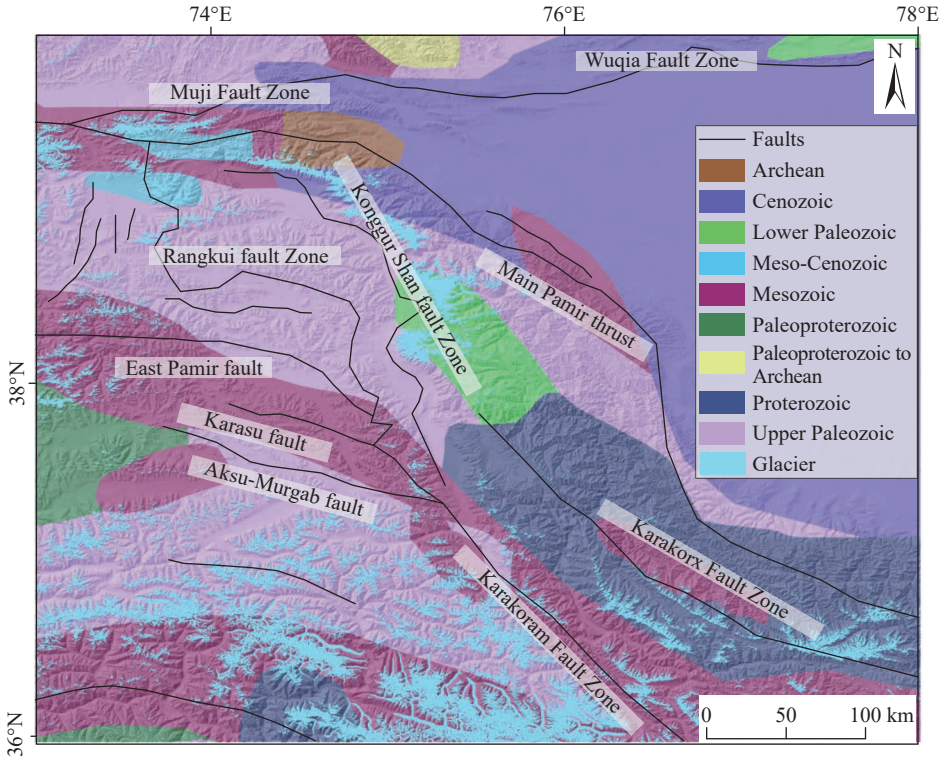

Fig. 2. Geological map of the study area.

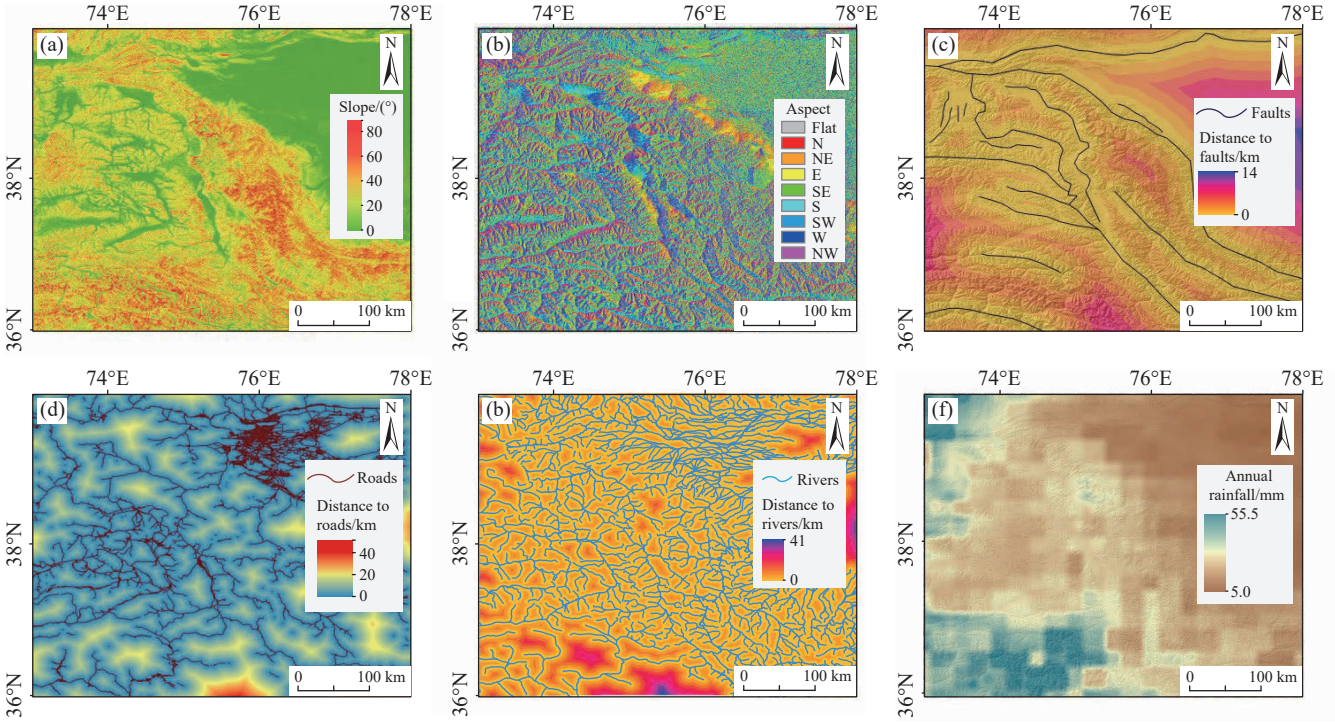

Fig. 3. Map of influencing factors: a–slope angle; b–slope aspect; c–distance to faults; d–distance to roads; e–distance to rivers; and f–annual precipitation.

feature platform depressions, accompanied by fissures along its middle and front edges; (3) irregular step-like distribution is shown on the landslide body; (4) in planar morphology, landslides are portrayed with a curved image resembling a "double ditch homologation"; (5) owing to early formation and significant scale, ancient landslides might have accommodated human habitation or cultivation; (6) the study area hosts numerous water systems. Landslides adjacent to these water systems may cause historical river-blocking events, in which the front edge potentially exhibits river extrusion phenomena (Sato HP and Harp EL, 2009; Ding H et al., 2011; Guzzetti F et al., 2012).

The authors conducted a comparative analysis between typical landslides found in this study and those documented in the literature and related research. Fig. 4 demonstrates a clear identification of typical landslides observed in the study area. Fig. 4a shows the location of typical landslides in the study area. Fig. 4b shows the Lymek landslide, featuring an expansive area of approximately 45×10^6 m^2. This landslide stretches between 10 km and 15 km from the top of the source area to the accumulation zone, showcasing an elevation variance of approximately 1225 m. Its movement direction is NE-trending. A comprehensive investigation of landslides has been conducted by interpretation of satellite images, field surveys and statistical analyses to analyse landslide morphology, internal lithological structure, and genesis mechanisms (Shi A et al., 2023). Fig. 4c shows the landslide body of Aerpa Aigezi, which has an area of approximately 78×10^4 m^2, a length of approximately 1500 m from the source area to the accumulation area, and a difference in elevation of approximately 971 m. The direction of landslide sliding is SE-trending. There is a clear phenomenon of landslides blocking the river. It has been studied in the direction of stratigraphic chronology and geologic lithology (Robinson AC et al., 2007; Yuan Z et al., 2013). Fig. 4d shows the Bulunkou landslide body, which has an area of approximately 2.8×10^6 m^2, a length of approximately 2200 m from its source to the accumulation area, and an elevation difference of approximately 708 m. The landslide sliding direction is SW-trending. There are signs of landslides blocking the river as well. The source area of the landslide is a Palaeozoic long quartz gneiss, which once blocked the tributary of the Muji River and was later cut through by the river (Robinson AC et al., 2004; Yuan Z, 2012; Yuan Z et al., 2013). Fig. 4e shows the Taheman landslide, with an area of approximately 5.4×10^6 m^2, a typical "tongue-shaped" morphology, a length of approximately 5200 m from the source area to the accumulation area, and a difference in elevation of approximately 1400 m. The direction of the landslide is SW-

Table 1. Data sources.

Data	Source	Website
DEM	ALOS PALSAR 12.5 m DEM	https://search.asf.alaska.edu/
geological map	China Geological Survey	
road and river	OpenStreetMap	https://www.openstreetmap.org
Rainfall (resolution 0.1°)	MSWEP dataset	https://www.gloh2o.org/mswep

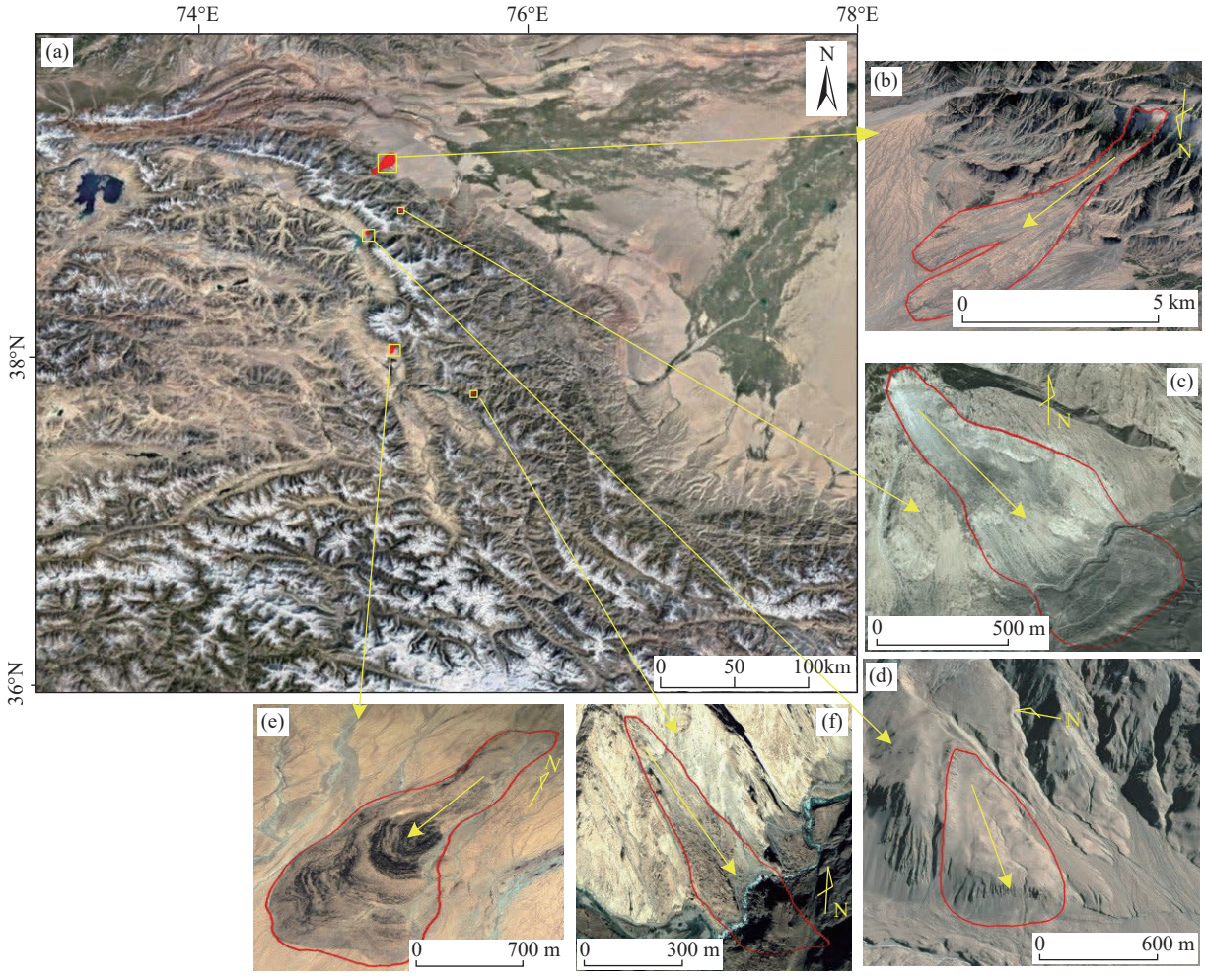

Fig. 4. Demonstration of typical landslides in the study area. a–Typical landslide locations in the study area; b–located at 75.16°E, 39.21°N; c–located at 75.24°E, 38.92°N; d–located at 75.04°E, 38.78°N; e–located at 75.19°E, 38.09°N; and f–located at 75.68°E, 37.82°N.

trending, with high mobility and a typical planar spilling long-runout landslide (Wang Y et al., 2019, 2020, 2021b). Fig. 4f shows the Bile Jiyi landslide, with an area of approximately 25×10^4 m^2. The length of the landslide from the source area to the accumulation area is approximately 1000 m. The difference in elevation is approximately 592 m. The sliding direction is ES-trending. The leading edge of the landslide washed up to approximately 80 m above the opposite slope, indicating that this landslide once blocked the Yarkand River landslide (Yuan Z, 2012; Yuan Z et al., 2013). Fig. 5 show field photos of several typical landslides from literatures. Fig. 5a–c show Iymek rock avalanche modified from Shi A et al. (2023) and correspond to Fig. 4b. Fig. 5d was modified from Yuan Z et al. (2013) and located at the southwest foot of Muztag Mountain with coordinates 75.11°E, 38.28°N. Fig. 5e–f show Bile Jiyi landslide modified from Yuan Z et al. (2013) and correspond to Fig. 4f. Fig. 5g shows Taheman landslide modified from Yuan Z et al. (2013) and correspond to Fig. 4e. Fig. 5h shows Bulunkou landslide modified from Yuan Z et al. (2013) and correspond to Fig. 4d. Fig. 5i show Attabad landslide occurred on January 4, 2010 modified from Gardezi H et al. (2021) with coordinates 74.82°E, 36.31°N.

4. Result and analysis

4.1. Distribution of landslides

There are 13003 recognizable landslides in the study area

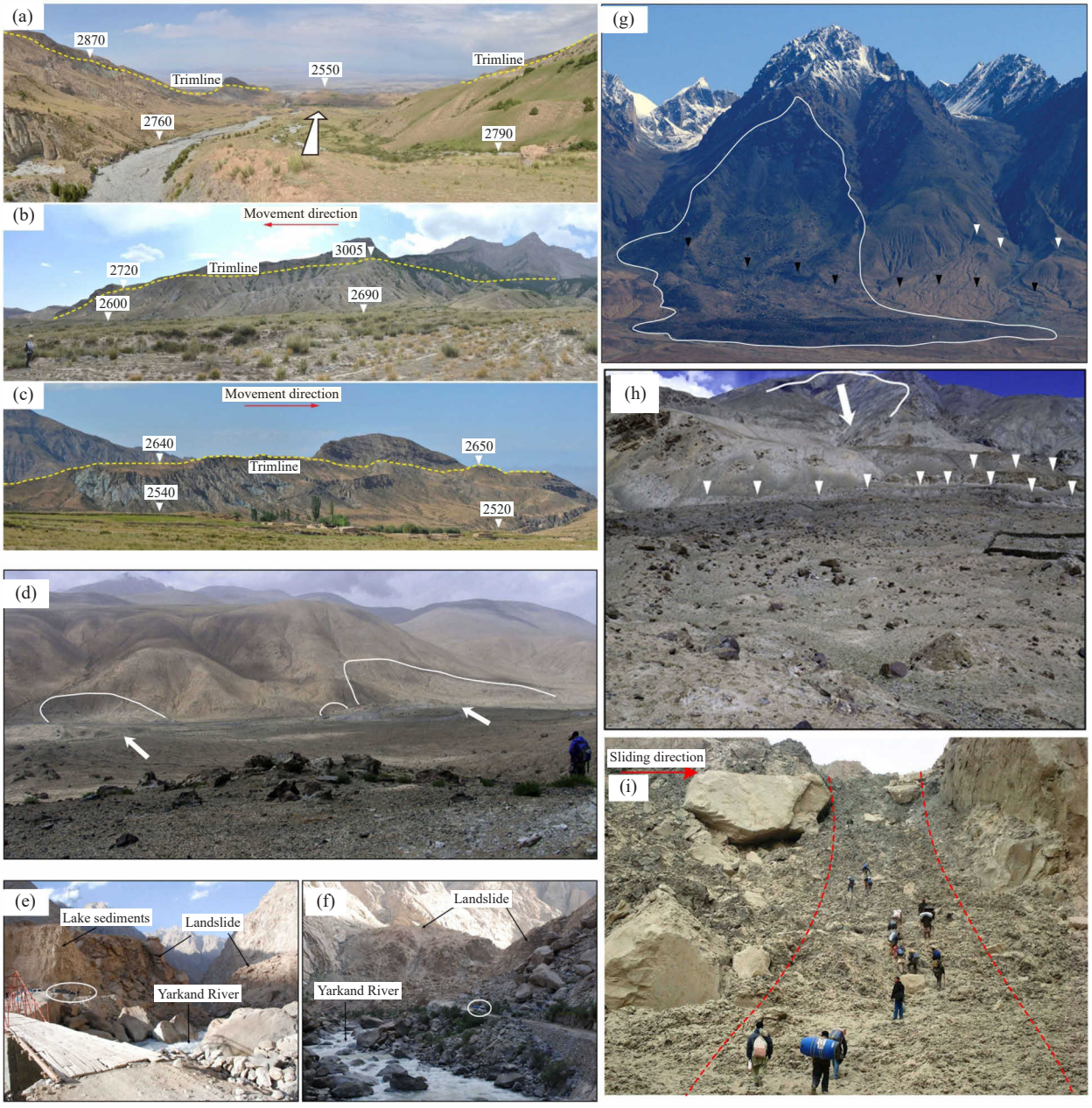

Fig. 5. Landslides photos on field. a–c–Iymek rock avalanche modified from Shi A et al. (2023); d–landslides located at the southwest foot of Muztag Mountain was modified from Yuan Z et al. (2013); e–f–parts of Bile Jiyi landslide modified from Yuan Z et al. (2013); g–Taheman landslide modified from Yuan Z et al. (2013); h–Bulunkou landslide modified from Yuan Z et al. (2013); i–a part of Attabad landslide modified from Gardezi H et al. (2021).

(see Fig. 6), and the total area of landslides is 3351.24 km^2. The individual landslide areas exhibit considerable variation, ranging from 0.01 km^2 to 45.29 km^2. Those landslides were divided into seven groups by area. Statistical analysis of the number of landslides and their corresponding areas within each group was conducted, as presented in Table 2. Approximately 45% of the total landslides were observed with landslide areas smaller than 0.1 km^2. Furthermore, the cumulative area of the landslide (those exceeding 1 km^2) was calculated as 1049.45km^2, accounting for 31% of total landslide area.

4.2. Relationship between impact factors and landslides

Based on the GIS platform, the authors computed the landslide areas and extracted corresponding environmental factors based on their locations. These factors encompass regional elevation, slope angle, slope aspect, distance to faults, distance to roads, distance to rivers, annual precipitation, and stratum. Employing these data, the authors conducted comprehensive statistical analyses, specifically, the number and area of landslides, LND, and LAP in the factor intervals (Fig. 7).

4.2.1. Influence of topographic factors

The elevation span across the study area ranges from 1403 m to 7893 m. To dissect the impact of elevation, this study categorised the landslides into groups based on elevation levels. The elevation of the main scarp of the landslide is used as the expression of the landslide elevation. The landslides with elevation less than 1500 m asl were categorised as a group, while those above 6000 m asl were categorised as a group. The intervening groups were spaced at 0.5 km intervals, resulting in a total of 11 groups. The relationship between elevation and key landslide metrics, including landslide count, total landslide area, LAP, and LND, was investigated (Fig. 7a). Most landslides were found within 4.5–5 km, with 2927 landslides, accounting for 22.51% of the total number of landslides. Below 5000 m altitude, the number of landslides increased with increasing elevation, while above 5 km, the number of landslides decreased with increasing elevation. The elevation range of the largest landslide area was also 4.5–5 km, with 1034.39 km^2, accounting for 30.87% of the total landslide area. The overall change in LND also showed an increasing and then decreasing trend, with a peak value of 15.7×10^6 km^2 at 5–5.5 km. This interval signified the highest concentration of landslides; the LAP achieved its peak value beyond the 5 km threshold, indicating that landslides covered the most substantial area in this range. Overall, the landslide distribution was most prominent at elevations above 4.5 km.

The slope angle in the study area ranges from 0–82°. Considering that both the average slope angle and the maximum slope angle significantly influenced the sliding of the landslide body when the landslide was triggered, both of the above indicators were counted in this study. The average slope angle refers to the average value of the slope grid over

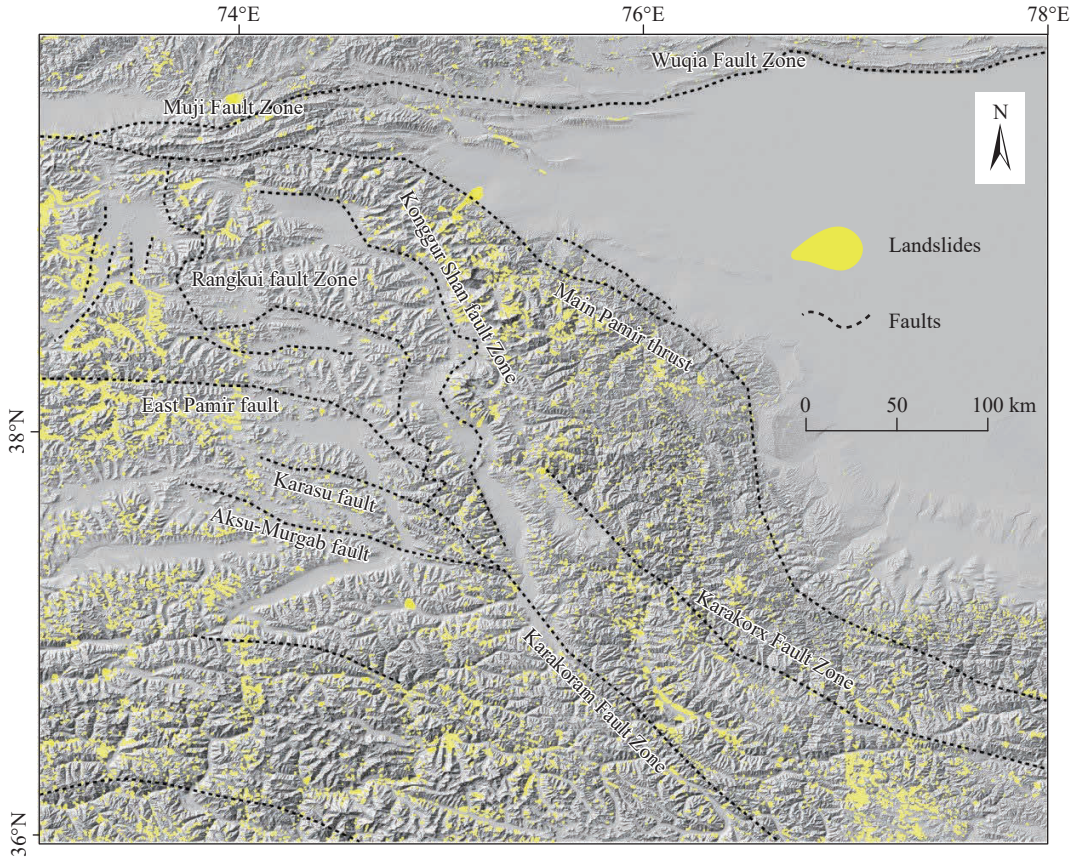

Fig. 6. Distribution of landslides in the study area.

Table 2. Grading statistics of landslide development.

Area of landslide/km^2	Num	Total area of landslides/km^2
<0.1	5842	276.25
0.1–0.2	2644	382.19
0.2–0.4	2398	676.37
0.4–0.6	904	439.77
0.6–0.8	456	315.47
0.8–1	237	211.74
>1	522	1,049.45

the landslide coverage area. The maximum slope angle is defined as the maximum slope of a single landslide area, whose value is the maximum value in the slope grid of the landslide coverage area.

The average slope angle across the region ranged between 5.61° and 77.58°. This study categorised the landslides into groups based on the average slope angle. Landslides with average slopes <10° were categorised as a group, while those >80° were categorised as a group. The intervening groups were spaced at 10° intervals, resulting in a total of nine groups. The relationship between the number of landslides, the area of landslides and the slope was analysed (Fig. 7b). The peak count of landslides, totalling 5490 instances or 42.22% of the aggregate, was identified within the 20° to 30° slope interval. At slopes <30°, the number of landslides increased with increasing slope. At slopes >30°, the number of landslides decreased with increasing slope. The area of landslides between 20° and 30° was the largest at 1352.50 km^2, accounting for 40.36% of the total landslide area. At slopes <30°, the landslide area increased with increasing slope. At slopes >30°, the landslide area decreased with increasing slope. Both LAP and LND showed the same trend and reached the maximum value at the 20° to 30° slope interval, which showed that landslide development predominantly prevailed in this range of average slopes.

The maximum slope angle across the region ranged between 9.99° and 85.64°. The landslides were categorised into nine groups based on maximum slope angle ranges: One group encompassing landslides with maximum slopes less than 10°, another for landslides exceeding 80°, and the rest grouped in 10° intervals in between. Fig. 7c shows the correlation between landslide count, landslide area, and slope. Slopes surpassing 80° housed the highest number of landslides at 4352, constituting 33.47% of the overall count. Correspondingly, the area occupied by these steep landslides stood at 1767.98 km^2, accounting for 52.76% of the total landslide area. This pattern demonstrated an upwards trend in landslide numbers and areas as slopes increased. This trend was consistent for both LAP and LND. Furthermore, this analysis underscores the concentration of landslide source areas within regions characterised by high slopes.

Slope aspects were categorised into eight zones: N, NE, E, SE, S, SW, W, and NW. This enabled an examination of the connection between landslide count and area concerning slope angle (see Fig. 7d). Among these zones, the highest landslide count, at 2607, representing 20.05% of the total, occurred when the slope angle was N. Conversely, when the slope angle was NE, the largest landslide area emerged, encompassing 630.28 km^2 and accounting for 18.81% of the total area. Both LND and LAP had high values in the N, NE and SW slope angle intervals. Therefore, it could be inferred that landslide occurrence primarily prevailed in areas with N-, NE-, and SW-oriented slopes. The five typical landslides illustrated in Fig. 4 all slid along the NE and SW directions.

4.2.2. Influence of geological and tectonic factors

The expansive study area is characterised by a dense convergence of faults. Acknowledging that the impact of faults on landslide distribution generally reduces with increasing distance, it follows that regions situated far from the faults experience less influence. Using 1 km intervals, the authors analysed the relationship between the number of landslides, landslide area, and distance from the faults, and landslides with distances greater than 15 km from the fault were categorised as a group, as shown in Fig. 7(e). The number of landslides was as high as 881 with an area of 219.53 km^2 when the fault distance was within 1 km. However, many landslides were also distributed in intervals larger than 15 km. In addition, the LND and LAP trends were complex, and it was difficult to find specific patterns. At present, many studies use the distance from the fault to indicate potential seismic activity (Havenith HB et al., 2015; Khan H et al., 2019; Kıncal C et al., 2009). The results of this paper indicates that some of the landslides in this region are not clearly related to faults, perhaps because some faults are very large in scope, or some old faults may not have been discovered at present.

The stratum of the study area included Archean, Cenozoic, Lower Paleozoic, Meso-Cenozoic, Mesozoic, Paleoproterozoic, Paleoproterozoic to Archean, Proterozoic, and Upper Paleozoic. In the process of researching geological data, the authors find that stratum of similar age often has relatively close rock and soil combinations, and a stratum may contain multiple lithologies. So, this study chooses the stratum as a statistical factor instead of lithologies. The relationship between the number of landslides, the area of landslides, and the stratum was analysed and shown in Fig. 7f. Mesozoic and Upper Paleozoic landslides were dominant, with counts of 5622 and 3874, constituting 43.24% and 29.79%, respectively. The corresponding areas spanned 1352.04 km^2 and 1229.83 km^2, accounting for 40.34% and 36.70%, respectively. LND and LAP showed similar trends, but higher values of LAP also existed in the Lower Paleozoic, which was mainly exposed in the central part of the study area by stratum, as shown in Fig. 2. The distribution of landslides was dominant in the above three stratum intervals.

4.2.3. Influence of hydrological and engineering factors

Roads in the study area are mainly located in the northeastern and southwestern margins, including railroads and highways. Since the construction or use of roads affects the surrounding soils and foundations, it can be assumed that

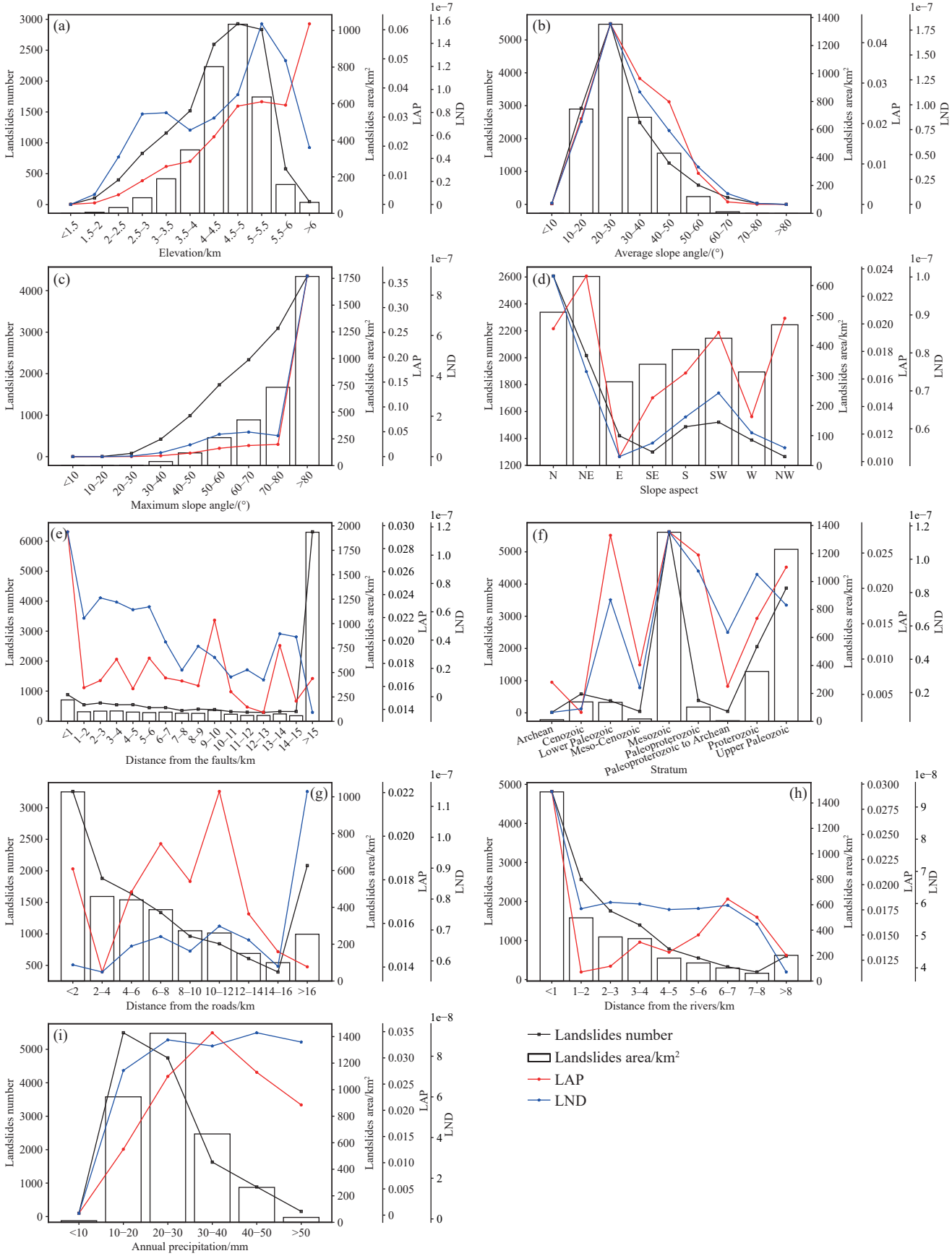

Fig. 7. Relationship between landslides and factors. a–Elevation; b–average slope angle; c–maximum slope angle; d–slope aspect; e–distance from the faults; f–stratum; g–distance from the roads; h–distance from the rivers; and i–annual precipitation..

human engineering activities can partially affect landslide triggers. Using 2 km intervals, the authors analysed the relationship between the number of landslides, landslide area, and distance from the roads, and landslides with distances greater than 16 km from the roads were categorised as a group, as shown in Fig. 7g. When within 2 km of a road, the landslide count surged to 3259, while the covered area extended to 1026.78 km^2. Conversely, in the interval spanning over 2 km but less than 16 km, a diminishing trend was evident in both landslide count and area, marked by fluctuating LND and LAP values. Beyond 16 km, the landslide count reached 2083. This trend mirrored the pattern observed in tectonic influences, indicating landslides influenced by human engineering activities within the study area.

Rivers are widely distributed in the study area. In this study, landslides more than 8 km from the rivers were categorised as a group using 1 km intervals, and the results of the analysis are shown in Fig. 7h. The most prominent occurrence of landslides, totalling 4819 and covering an area of 1487.20 km^2, materialised when situated within 1 km of rivers. LND and LAP increased in the interval of 6–7 km from rivers, indicating that there were some landslide-intensive areas in this interval. However, in general, the intervals within 1 km from the rivers had a clear advantage over other intervals.

The overall low rainfall in the study area is related to its original location in the hinterland of the Eurasian continent, which is mainly influenced by the westerly wind belt and therefore has an arid and semiarid climate. With rainfall graded at 10 mm, landslides with rainfall greater than 50 mm were categorised as a group. The authors analysed the relationship between the number of landslides, landslide area, and rainfall, as shown in Fig. 7i. The most substantial landslide occurrence, totalling 5496, was noted when rainfall ranged from 10 mm to 20 mm. The most extensive landslide-covered area, spanning 1425.85 km^2, was observed within the 20 mm to 30 mm rainfall range. The trend in LND and LAP indicated elevated values within the 20 mm to 30 mm and 30 mm to 40 mm rainfall ranges.

4.3. Geometric and morphological characteristics of landslides

Regarding the geometric and morphological attributes of landslides, the investigation in this study centred on using the ratio between height drop (H), vertical distance between the headscarp crown and the deposits tip, and length (L) (Strom A and Abdrakhmatov K, 2018). This ratio, recognised as the equivalent friction coefficient, serves as a pivotal parameter in exploring regional landslide morphology, as well as landslide mechanics and mobility. The calculation procedure for H and L, elucidated through a visual representation in Fig. 8, is as follows. To ascertain the value of H, this study extract elevation data within the spatial extent of the landslide. The disparity between the highest and lowest values in these raster data defines H. The computation of L entails generating the minimum enclosing circle based on the extent of the landslide. The diameter of this circle is subsequently adopted as the value of L. This approach to characterising landslides based on H and L is essential for understanding their morphological intricacies and regional behaviour.

The statistical results are shown in Fig. 9. The values of H in the study area were mainly concentrated in the range of 200–600 m, and the maximum value of the height difference reached 3115 m. Furthermore, L were predominantly concentrated between 500–1500 m, with the greatest distance reaching 16325 m. In the present study area, the ratios of H/L were primarily distributed between 0.4 and 0.64. Furthermore, earlier investigations have indicated a correlation between H and L following a power law or linear relationship (Hattanji T and Moriwaki H, 2009; Guo C et al., 2016). In this study, the

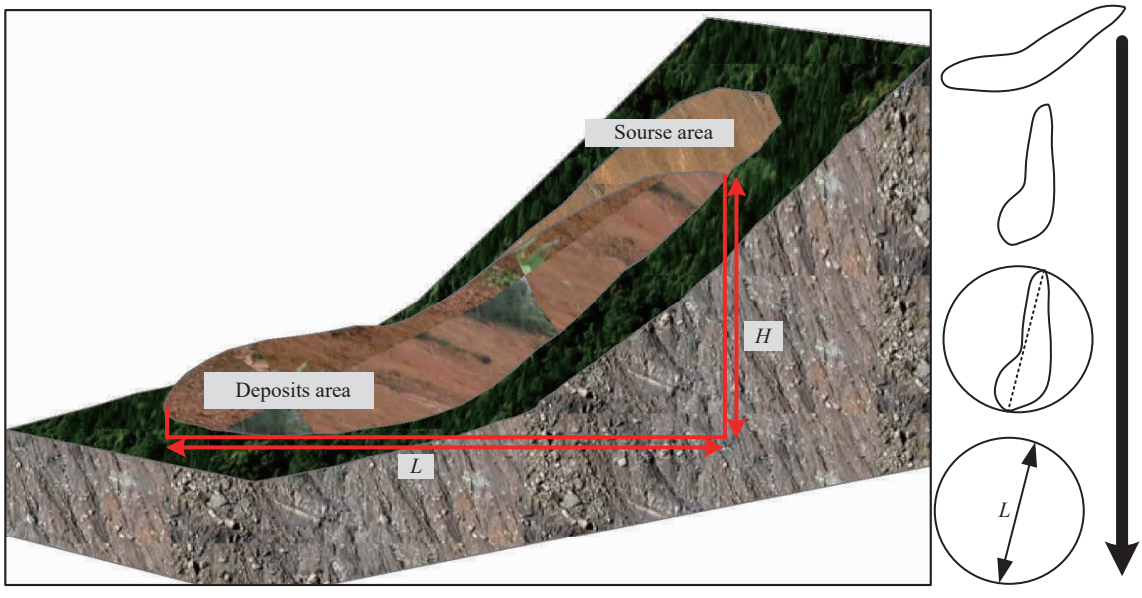

Fig. 8. Landslide H/L Schematic.

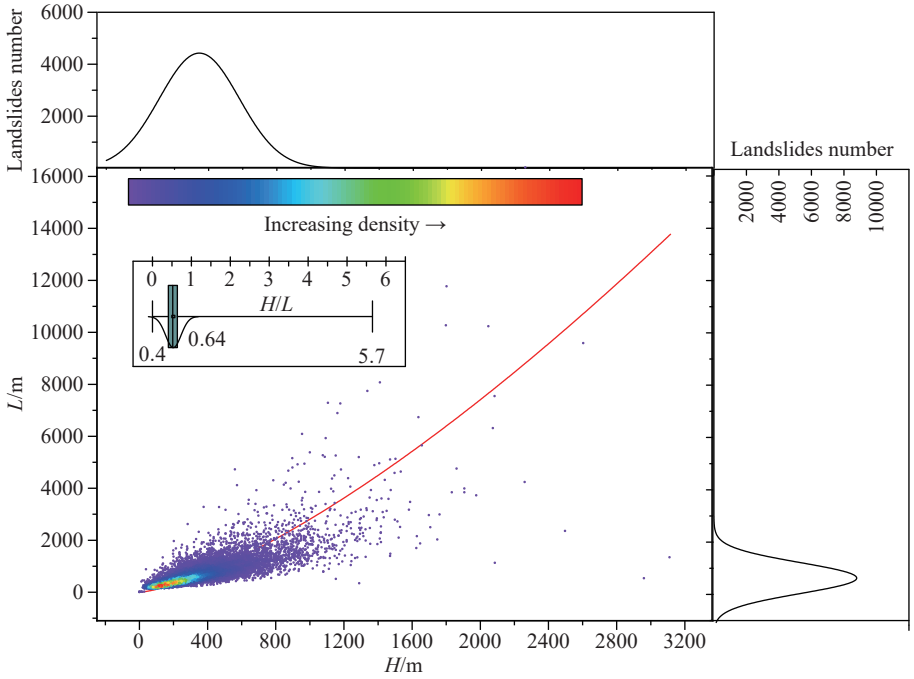

Fig. 9. Landslide *H*-*L* relationship diagram.

authors adopted the Allometric model to fit the power law relationship between *H* and *L*, as described in Equ. 1.

$$L = 0.17 * H^{1.4} \quad (1)$$

The function image is shown as the red line in Fig. 9.

Summarising the geometric and morphological attributes of landslides within this study area and elucidating the relationship between landslide height difference and slip distance are valuable for comprehending landslide mobility traits and aiding future predictions. In this study, the authors established that the relationship between the landslide height difference and slip distance follows a power law pattern. This power law model more aptly characterises landslides within this study area, as opposed to the linear relationship seen in earlier investigations (Zhao B et al., 2021; Zhang X et al., 2022).

Employing a GIS platform, the authors extracted ridgelines in the study region and calculated the distances from landslides to these ridgelines. Building on the findings of slope analysis, this study deduced that the primary concentration of landslide source areas corresponds to regions with high slope angles, typically near the ridgelines. To delve deeper into landslide distribution on mountain slopes, the authors constructed Fig. 10. Given that certain landslides are distanced considerably from water systems and river valleys, significantly deviating from the average (as depicted in Fig. 7), such cases can create substantial statistical outliers. Hence, the authors exclusively considered landslides within an 8 km radius of rivers for statistical analysis. This subset accounted for 95% of the total landslide count, ensuring that the results mirrored the general distribution pattern in the study area. Fig. 10 features the relative distance from the summit of the slope (i.e., the ridge) to the landslide apex on the horizontal axis and the relative distance from the landslide's leading edge to the base of the slope (i.e., the river valley) on the vertical axis. Hollow circles of varying diameters represent landslides of different sizes, and the colour map indicates the density of landslide occurrences. Analysis of Fig. 10 revealed two primary zones of landslide concentration. Where the relative distance from the ridge was within 0–0.2 and the relative distance from the rivers ranged from 0.6 to 1. This means most of the landslides in the study area are distributed on high slopes.

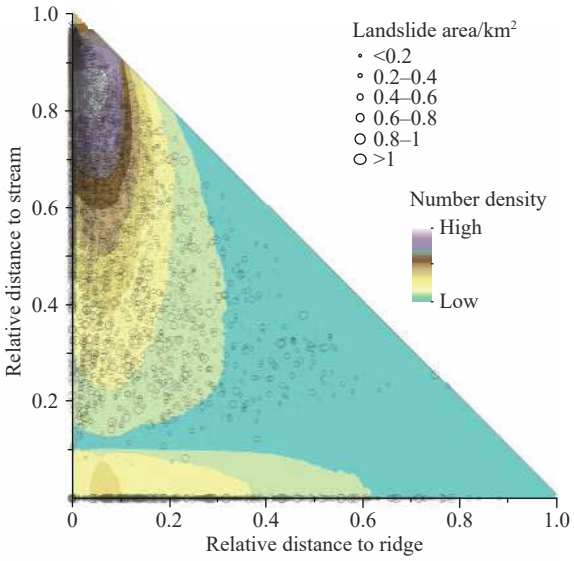

Fig. 10. Location of landslides with respect to ridges and streams.

5. Discussion

5.1. Significance of the landslide database

Cataloguing recognizable landslides in the northwest margin of the Qinghai-Tibet Plateau can help us gain a

comprehensive understanding of the distribution and characteristics of landslides in the region. This is important for studying the formation mechanism, scale and frequency of landslides, which helps to reveal the potential risks and hazards of geohazards. In this study, a recognizable landslide database for the region was established using the human-computer interaction interpretation method (researcher operate computer combining GIS platform and remote sensing image to identify landslides). Compared with the automatic landslide recognition method, this method has higher precision. The complete boundary of landslides can be obtained based on artificial visual interpretation, and the wrong judgment of landslides can be reduced based on high resolution image. And more efficient than field work. Compared with the existing landslide database (Zheng S et al., 2018; Zhao B et al., 2019; Qi T et al., 2021), this catalogued map has a wider regional scope and fills in the missing cases of possible new landslide activities or historical landslides in the northwest margin of the Qinghai-Tibet Plateau. By performing a new cataloguing exercise, landslide data can be updated in a timely manner to enhance the data's accuracy and reliability.

However, there are some limitations in the current interpretation results. The remote sensing interpretation of significant landslides in the northwestern margin of the Qinghai-Tibet Plateau contends with a range of influencing factors: The region's lofty altitudes and intricate topography, combined with glacial and seasonal snow coverage, dense vegetation, varied lithology, soil types, and geological activities. The intricate topography characterised by elevated terrains and steep relief presents a distinct challenge to remote sensing interpretation. This is particularly pronounced due to potential shadows, distortions, and elevation fluctuations in remotely acquired imagery, potentially obscuring landslide boundaries and distinctive features. In addition, the prevalence of glaciers and seasonal snow cover in the northwest corner increases the complexity. The presence of these glacial features and snow cover introduces challenges in landslide interpretation, as they can conceal or alter geomorphic attributes of landslides, thus impeding accurate determination of their boundaries and dimensions. Additionally, the presence of dense vegetation within the region introduces further complexities to landslide interpretation. Vegetation cover may obscure or veil landslides' distinctive geomorphic traits, contributing to challenges in accurately delineating their boundaries and morphology. Moreover, different lithologies and soil types can impact landslide formation and evolution, but they may exhibit similar spectral characteristics in remote sensing images, complicating the process of landslide identification and classification. Importantly, this research methodology heavily relied on satellite imagery. The extent of satellite coverage, image quality, and the timing of image capture can limit this research endeavours. In addition, better results can be obtained by conducting field work (Xu C et al., 2019; Cui Y et al., 2020; Ma S et al., 2021).

5.2. Discussion on impact factors and landslide

On the basis of landslide inventory, the relationship between landslide distribution and three types of environmental factors was analysed: Topography, geology and tectonics, and hydrology and engineering. Considering the study area's geographical, topographical and geomorphic characteristics, and by means of comparative analysis, the underlying rationales for the observed relationships were examined as follows.

Elevation determines the geomorphologic type, and there are some differences in vegetation cover and soil moisture in different elevation intervals. Notably, elevations surpassing 4.5 km were the predominant intervals for landslide distribution in this study. This phenomenon could be attributed to the region's higher overall topography. Importantly, the dominant elevation interval for landslide development is significantly larger relative to the Loess Plateau area (Hu S, 2019; Chen Y et al., 2022) and the southwestern mountainous area (Li L et al., 2022). Slope, representing the degree of surface steepness, partly dictates the critical threshold for landslide initiation. In this study, the relationship between the number of landslides and slope is consistent with the conclusion of Xu C et al. (2014b). Slope aspects plays an important role in mountain ecology, so it affects the occurrence of landslides. In this study, when the slope aspect is N, the largest number of landslides are observed. Li L et al. (2022) attributed the phenomenon of more landslides in some slope aspects to the influence of river erosion.

Both active faults and earthquakes can significantly impact landslide formation and development by triggering changes in surface stress, vibrations, and disruption of geotechnical structures. In this study, it was observed that the spatial distribution of landslides is not greatly impacted by faults. This aligned with the findings of a prior investigation (Chen Y et al., 2022), possibly due to the substantial time elapsed since landslide events and the prolonged exposure to weathering, erosion, and geomorphic processes. These factors have potentially obscured the original surface characteristics of landslides, hindering a correlation with active faults. Xu Y et al. (2022) found that, in comparison to other types of landslides, landslides triggered by earthquakes can still exhibit noticeable signs for hundreds or even thousands of years. These landslides serve as records of earthquake ground motion in the region. In the eastern Pamir Plateau, there are numerous landslides and rockfalls. The prominent characteristics of these rock avalanches include wedge-shaped damage patterns within jointed groups and well-defined deep-seated scars featuring nearly planar main scarps (Shi A et al., 2023). The analysis identifies seismic activity, notably earthquakes, as the primary triggering factor for significant landslides and rockfalls in this region, which is consistent with Robinson TR et al.'s (2015) findings. Research conducted by Yuan Z et al. (2013) delved into sizeable landslides within the active orogenic belt of the Pamir region.

This investigation highlighted that the source areas of these landslides predominantly consist of metamorphic rocks, prone to weathering and fragmentation, with well-developed slices or joints. The study concluded that the interplay between pore water pressure and seismic events significantly influences landslide occurrence in this region. The present study's analysis of landslide distribution also revealed a concentration within tectonically proximate regions and high-frequency seismic zones, aligning with established triggering mechanisms observed in prior research. The geological composition, specifically stratum, emerges as a substantial factor influencing landslide development, serving as the foundational material for landslide incidents. Unlike some recent studies (Li L et al., 2021), the study area in question is positioned within a highly weathered high mountain canyon region, where landslides predominantly manifest within Mesozoic and Upper Paleozoic outcrops. This study chooses the stratum as a statistical factor. In fact, lithology does have a finer classification in engineering geological analysis. In the process of researching geological data, the authors observe that a stratum may contain multiple lithologies. For regional large-scale landslides, especially deep-strata landslides, it is not enough to consider only the single lithology of the surface layer. At the same time, it may be difficult to measure the engineering geological strength of each landslide in practice. In addition, even if the lithology is the same, factors such as formation time, burial depth and overburden pressure will also affect the engineering geological characteristics. The authors find that stratum of similar age often has relatively close rock and soil combinations. This is consistent with the original intention of statistical analysis of landslide development through different factor intervals. This choice helps to reveal the law of landslide development more comprehensively, and also takes into account the feasibility of practical operation. Meanwhile, there are some limitations to this approach, and the authors will continue to pay attention to the importance of lithology and engineering geological rock group in engineering geological analysis.

During road construction, activities such as excavation, slope cutting, paving, and loading induce stress redistribution on slopes, thereby facilitating landslides. This study encompassed a substantial area where road-associated landslides are influenced by human engineering interventions. River distribution is crucial for landslide evolution, as rivers manifesting through groundwater infiltration and soil erosion at slope bases contribute to landslide propagation. The highest landslide frequency in this study was observed within 1 km of rivers, corroborating the findings of Li L et al. (2022) in a comparable alpine valley. Rainfall, a pivotal contributor to surface water and groundwater recharge, holds significance. However, since most investigated landslides occurred in the past (Xu Y et al., 2020), discerning a clear connection between rainfall and current landslide distribution patterns is challenging.

When analysing the relationship between landslide distribution and environmental factors, the focus remained on individual factor-landslide associations. The limitation of this study was the absence of extensive exploration into distribution characteristics arising from the combined influence of multiple factors. By contrast, machine learning models for landslide susceptibility evaluation (Bui DT et al., 2012; Xu C et al., 2012b, 2016; Chen W et al., 2018) tend to incorporate weightings for diverse factors, considering their collective impact.

5.3. Discussion on Geometric and morphological characteristics of landslides

Most high-speed long runout landslides have apparent friction coefficients of 0.1–0.3 (Wang Y et al., 2017, 2018). Some have H/L>0.3， for instance, Aoraki/Mount Cook landslides (Cox SC et al., 2015), Val Pola landslides (Govi M et al., 2002), Huaying Mountain Xikou landslides (Jiang Y and Yin J, 1992). In the present study area, the ratios of H/L were primarily distributed between 0.4 and 0.64. This suggested liquidity is relatively low of landslides in this region.

In terms of triggering factors, landslides triggered by earthquakes or more heavily affected by earthquakes have higher H/L values than precipitation-type landslides at the same scale (Fan X et al., 2012). Zhuang J et al. (2022), taking the non-earthquake triggered landslide of the whole Loess Plateau as the research object, concluded that the H/L value is concentrated in the range of 0.2-0.4. Zhang X et al. (2022) statistically analyzed the ancient landslide in Luliang City, Shanxi Province, which is a typical landform of the Loess Plateau. There are few historical earthquakes, and the results show that the landslide H/L is concentrated in 0.2–0.25. Tian Y et al. (2020) analyzed the coseismic landslide triggered by the 2015 Nepal earthquake, and the average H/L of the landslide was 0.7. According to Yin Z et al. (2022), for the large landslide in Maoxian County, Sichuan Province, China in 2017, it was located in meizoseismal area and was affected by two large earthquakes. The calculated equivalent friction angle was 23°, and the H/L value after conversion was 0.42. Zhao et al. (2021) analyzed the form of coseismic landslide triggered by the 2018 Palu earthquake in Indonesia, and the results showed that the average H/L of coseismic landslide in mountainous areas was 0.56. Shao X et al. (2020) analysis of landslides in Yunnan Province in southwest China shows that the average H/L is 0.45–0.5, and the seismic activity in this region is very strong. Based on the comparison of the above studies, although there is no definitive conclusion at present, the authors preliminarily conclude that in terms of morphological characteristics, landslides in the study area may be more similar to landslides triggered by earthquakes or located in meizoseismal area.

The method adopted in this study is one of the widely used methods in current research (Tian Y et al. 2017; Rana K et al. 2021), which is determined by the external geometry of the plane morphology of the landslide. Some studies have shown that this method is feasible, although there may be

some errors, it will not affect the general law obtained in the study. In addition, all the landslides in the study area are large-scale landslides with a long formation time. After a long evolution, the shape tends to be regular. The workload of manual measurement is relatively large. There are very few landslides turns in the sample, and the results obtained by this model are reliable. Other methods are also practical, such as a research result by Li L et al. (2020, 2022), which proposed a new approach for measuring path-dependent landslide length, width, and aspect ratio. In addition, there are many studies that can be done on the geometric characteristics of landslides, such as the study by Strom A and Abdrakhmatov K (2018) on the correlation of volume, area of the deposits, affected area, height drop, runout characterizing, and so on.

6. Conclusions

Focused on the recognizable landslides in the northwest margin of the Qinghai-Tibet Plateau, a comprehensive analysis on distribution and characteristics is conducted with the following main conclusions being achieved.

(i) A complete landslide database is provided in the study area. A total of 13003 landslides were identified in the study area, spanning from 36°N to 40°N latitude and 73°E to 78°E longitude. The total area is 3351.24 km^2.

(ii) The characteristics of landslide spatial distribution is revealed. Situated in a severely weathered alpine canyon setting, the study area's geological composition primarily comprises Mesozoic and Upper Paleozoic outcrops. Landslide development is most dominant in the elevation interval above 4.5 km, in the average slope angle interval of 20°–30°, in the maximum slope angle interval above 80°, in the slope aspects interval of N, NE and SW, and distance to rivers below 1 km, rainfall between 20–30 mm and 30–40 mm. Tectonic movements and seismic events predominantly govern landslide occurrence, although some are influenced by human engineering activities.

(iii) Geometric and morphological characteristics of landslides is revealed. The landslide H/L ratios in the study area are mainly concentrated between 0.4 and 0.64. The landslide mobility in the region is relatively low, and the landslide height difference is a power-law fit to the slip distance. And the authors preliminarily conclude that in terms of morphological characteristics, landslides in the study area may be more similar to landslides triggered by earthquakes or located in meizoseismal area. A location map of regional landslides in terms of relative distance from ridges and river valleys was drawn, indicating that most of the landslides in the study area are distributed on high slopes.

The authors provide a detailed analysis of landslides' spatial distribution within the study area. Future work can expand into the classification, susceptibility assessment, and hazard assessment of these landslides. These works offer a scientific foundation and support for disaster prevention, mitigation efforts, and decision-making in emergency management.

CRediT authorship contribution statement

Chong Xu conceived of the presented idea. Yu-long Cui, Shuai Wu, Zhi-qiang Yang, Kai Ma contributed to the core data preparation. Xiao-yi Shao, Lei Li, Li-ye Feng, Hui-ran Gao analyzed the result. Wei Wang and Yuan-dong Huang wrote the manuscript with support from Chong Xu. All authors discussed the results and contributed to the final manuscript.

Declarations of interest

The authors declare no conflicts of interest.

Acknowledgement

The authors thank the reviewers and editors who participated in the manuscript review. This research was supported by the National Key Research and Development Program of China (2021YFB3901205) and National Institute of Natural Hazards, Ministry of Emergency Management of China (2023-JBKY-57).

References

Borgatti L, Soldati M. 2010. Landslides as a geomorphological proxy for climate change: A record from the Dolomites (northern Italy). Geomorphology, 120(1–2), 56–64. doi: 10.1016/j.geomorph.2009.09.015.

Brunel M, Arnaud N, Tapponnier P, Pan Y, Wang Y. 1994. Kongur Shan normal fault: Type example of mountain building assisted by extension (Karakoram fault, eastern Pamir). Geology, 22(8), 707–710. doi: 10.1130/0091-7613(1994)022<0707:ksnfte>2.3.co;2.

Bui DT, Pradhan B, Lofman O, Revhaug I. 2012. Landslide susceptibility assessment in vietnam using support vector machines, decision tree, and naïve bayes models. Mathematical Problems in Engineering, 2012, 1–26. doi: 10.1155/2012/974638.

Chen W, Peng J, Hong H, Shahabi H, Pradhan B, Liu J, Zhu AX, Pei X, Duan Z. 2018. Landslide susceptibility modelling using GIS-based machine learning techniques for Chongren county, Jiangxi Province, China. Science of The Total Environment, 626, 1121–1135. doi: 10.1016/j.scitotenv.2018.01.124.

Chen Y, He X, Xu C, Huang Y, Zhang P, Luo Z, Zhan T. 2022. Development characteristics and causes of a fatal landslide occurred in Shuicheng, Guizhou Province, China. ISPRS International Journal of Geo-Information, 11(2), 119. doi: 10.3390/ijgi11020119.

Chen Z, Huang Y, He X, Shao X, Li L, Xu C, Wang S, Xu X, Xiao Z. 2023. Landslides triggered by the 10 June 2022 Maerkang Earthquake Swarm, Sichuan, China: Spatial distribution and tectonic significance. Landslides. doi: 10.1007/s10346-023-02080-0.

Chevalier ML. 2019. Active tectonics along the Karakorum Fault, western Tibetan Plateau: A review. Acta Geoscientica Sinica, 40(1), 37–54. doi: 10.3975/cagsb.2018.101601.

Cox SC, McSaveney MJ, Spencer J, Allen SK, Ashraf S, Hancox GT, Sirguey P, Salichon J, Ferris BG. 2015. Rock avalanche on 14 July 2014 from Hillary Ridge, Aoraki/Mount Cook, New Zealand. Landslides, 12, 395–402. doi: 10.1007/s10346-015-0556-7.

Cui P, Su F, Zou Q, Chen NS, Zhang Y. 2015. Risk assessment and disaster reduction strategies for mountainous and meteorological hazards in Tibetan Plateau. Chinese Science Bulletin, 60(32), 3067–3077 (in Chinese). doi: 10.1360/n972015-00849.

Cui Y, Bao P, Xu C, Fu G, Jiao Q, Luo Y, Shen L, Xu X, Liu F, Lyu Y,

Hu X, Li T, Li Y, Liu Y, Tian Y. 2020. A big landslide on the Jinsha River, Tibet, China: Geometric characteristics, causes, and future stability. Natural Hazards, 104(3), 2051–2070. doi: 10.1007/s11069-020-04261-9.

Cui Y, Yang W, Xu C, Wu S. 2023. Distribution of ancient landslides and landslide hazard assessment in the western Himalayan Syntaxis area. Frontiers in Earth Science, 11, 1135018. doi: 10.3389/feart.2023.1135018.

Deng J, Han F, Li T, Zhang B, Xu J, Yao Y. 2020. Late-Quaternary slip sense and rate of the Muji fault, northeastern Pamir. Quaternary Sciences, 40(1), 114–123 (in Chinese). doi: 10.11928/j.issn.1001-7410.2020.01.11.

Dewitte O, Chung CJ, Demoulin A. 2006. Reactivation hazard mapping for ancient landslides in West Belgium. Natural Hazards and Earth System Sciences, 6, 653–662. doi: 10.5194/nhess-6-653-2006.

Ding H, Zhang M, Li L. 2011. Interpreting landslides in the northwestern Loess Plateau using remote sensing images. Quaternary Sciences, 31(6), 1077–1085 (in Chinese). doi: 10.3969/j.issn.1001-7410.2011.06.15.

Fan X, Qiao J, Han M, Zeng Y. 2012. Volumes and movement distances of earthquake and rainfall-induced catastrophic landslides. Rock and Soil Mechanics, 33(10), 3051–3058 (in Chinese). doi: 10.16285/j.rsm.2012.10.016.

Fu W, Wang J, Liu S. 2003. Studies on the distribution rule of ground temperatures in Tarim Oilfield. Journal of Arid Land Resources and Environment, 17(6), 99–102 (in Chinese). doi: 10.13448/j.cnki.jalre.2003.06.019.

Gardezi H, Bilal M, Cheng Q, Xing A, Zhuang Y, Masood T. 2021. A comparative analysis of Attabad landslide on January 4, 2010, using two numerical models. Natural Hazards, 107(1), 519–538. doi: 10.1007/s11069-021-04593-0.

Georgi F, Krastanov M. 2015. Evaluation of the Possibilities for Construction on Ancient Landslide. Engineering Geology for Society and Territory, 2, 267–271. doi: 10.1007/978-3-319-09057-3_39.

Govi M, Gullà G, Nicoletti PG. 2002. Val Pola rock avalanche of July 28, 1987, in Valtellina (Central Italian Alps). Geological Society of America Reviews in Engineering Geology, XV, 71–89.

Guo C, Zhang Y, Montgomery DR, Du Y, Zhang G, Wang S. 2016. How unusual is the long-runout of the earthquake-triggered giant Luanshibao landslide, Tibetan Plateau, China? Geomorphology, 259, 145–154. doi: 10.1016/j.geomorph.2016.02.013.

Guzzetti F, Mondini AC, Cardinali M, Fiorucci F, Santangelo M, Chang KT. 2012. Landslide inventory maps: New tools for an old problem. Earth-Science Reviews, 112(1–2), 42–66. doi: 10.1016/j.earscirev.2012.02.001.

Hattanji T, Moriwaki H. 2009. Morphometric analysis of relic landslides using detailed landslide distribution maps: Implications for forecasting travel distance of future landslides. Geomorphology, 103(3), 447–454. doi: 10.1016/j.geomorph.2008.07.009.

Havenith HB, Torgoev A, Schlögel R, Braun A, Torgoev I, Ischuk A. 2015. Tien Shan Geohazards Database: Landslide susceptibility analysis. Geomorphology, 249, 32–43. doi: 10.1016/j.geomorph.2015.03.019.

Hu S. 2019. Spatial pattern of landslide in Loess Plateau and its influence on geomorphologic evolution. Xi'an, Northwest University, Ph. D thesis, 1–230 (in Chinese).

Huang Y, Xu C, Li L, He X, Cheng J, Xu X, Li J, Zhang X. 2023. Inventory and spatial distribution of ancient landslides in Hualong county, China. Land, 12(1), 136. doi: 10.3390/land12010136.

Jiang Y, Yin J. 1992. Huaying Mountain Xikou landslide-debris flow. Geological Hazards and Environment Preservation, 3(2), 51–58 (in Chinese).

Khan H, Shafique M, Khan MA, Bacha MA, Shah SU, Calligaris C. 2019. Landslide susceptibility assessment using Frequency Ratio, a case study of northern Pakistan. The Egyptian Journal of Remote Sensing and Space Sciences, 22, 11–24. doi: 10.1016/j.ejrs.2018.03.004.

Kıncal C, Akgun A, Koca MY. 2009. Landslide susceptibility assessment in the Izmir (West Anatolia, Turkey) city center and its near vicinity by the logistic regression method. Environmental Earth Sciences, 59, 745–756. doi: 10.1007/s12665-009-0070-0.

Kohno M, Yuki H. 2023. Landslide susceptibility assessment in the Japanese Archipelago based on a landslide distribution map. ISPRS International Journal of Geo-Information, 12(2), 37. doi: 10.3390/ijgi12020037.

Li L, Lan H, Strom A. 2020. Automatic generation of landslide profile for complementing landslide inventory. Geomatics, Natural Hazards and Risk, 11(1), 1000–1030. doi: 10.1080/19475705.2020.1766578.

Li L, Lan H, Strom A, Macciotta R. 2022. Landslide length, width, and aspect ratio: Path-dependent measurement and a revisit of nomenclature. Landslides, 19, 3009–3029. doi: 10.1007/s10346-022-01935-2.

Li L, Xu C, Yao X, Shao B, Ouyang J, Zhang Z, Huang Y. 2022. Large-scale landslides around the reservoir area of Baihetan hydropower station in southwest China: Analysis of the spatial distribution. Natural Hazards Research, 2(3), 218–229. doi: 10.1016/j.nhres.2022.07.002.

Li L, Xu C, Zhang Z, Huang Y. 2021. Spatial distribution and its control factors of landslides in Longxi County, Gansu Province, China. IOP Conference Series: Earth and Environmental Science, 861(5), 052013. doi: 10.1088/1755-1315/861/5/052013.

Li W. 2013. Active structure and strong earthquake in Tashkurgan valley, Northeast Pamir Plateau. Beijing, Institute of Geology, China Earthquake Administration, Ph. D thesis, 1–132 (in Chinese).

Ma D, Cui P, Yang K, Wang Z. 2003. Road hazards of the segment of Xinjiang-Tibet highway in Xinjiang and their primary cause analysis. Journal of Natural Disasters, 12(3), 93–98 (in Chinese).

Ma S, Xu C. 2019. Assessment of co-seismic landslide hazard using the Newmark model and statistical analyses: A case study of the 2013 Lushan, China, Mw6. 6 earthquake. Natural Hazards, 96(1), 389–412. doi: 10.1007/s11069-018-3548-9.

Ma S, Xu C. 2021. The monitoring of a large ancient landslide in Sichuan Province, China, using interferometric synthetic aperture radar technology and sensitivity analysis in potential landslide mass modeling. IOP Conference Series:Earth and Environmental Science, 861(5), 052009. doi: 10.1088/1755-1315/861/5/052009.

Ma S, Xu C, Shao X, Xu X, Liu A. 2021. A large old landslide in Sichuan Province, China: surface displacement monitoring and potential instability assessment. Remote Sensing, 13(13), 2552. doi: 10.3390/rs13132552.

Nilsen TH, Turner BL, Geological Survey (U. S.). 1975. Influence of Rainfall and Ancient Landslide Deposits on Recent Landslides (1950-71) in Urban Areas of Contra Costa County, California. California, U. S. Government Printing Office, 1–18.

Pánek T, Hradecký J, Smolková V, Šilhán K. 2008. Giant ancient landslide in the Alma water gap (Crimean Mountains, Ukraine): notes to the predisposition, structure, and chronology. Landslides, 5, 367–378. doi: 10.1007/s10346-008-0129-0.

Parker RN, Densmore AL, Rosser NJ, de Michele M, Li Y, Huang R, Whadcoat S, Petley DN. 2011. Mass wasting triggered by the 2008 Wenchuan earthquake is greater than orogenic growth. Nature Geoscience, 4(7), 449–452. doi: 10.1038/ngeo1154.

Qi T, Meng X, Qing F, Zhao Y, Shi W, Chen G, Zhang Y, Li Y, Yue D, Su X, Guo F, Zeng R, Dijkstra T. 2021. Distribution and characteristics of large landslides in a fault zone: A case study of the NE Qinghai-Tibet Plateau. Geomorphology, 379, 107592. doi: 10.1016/j.geomorph.2021.107592.

Qi W, Yang W, He X, Xu C. 2021. Detecting Chamoli landslide

precursors in the Southern Himalayas using remote sensing data. Landslides, 18(10), 3449–3456. doi: 10.1007/s10346-021-01753-y.

Rana K, Ozturk U, Malik N. 2021. Landslide geometry reveals its trigger. Geophysical Research Letters, 48(4), e2020GL090848. doi: 10.1029/2020GL090848.

Rao G, Cheng Y, Lin A, Yan B. 2017. Relationship between landslides and active normal faulting in the epicentral area of the AD 1556 M~8.5 Huaxian earthquake, SE Weihe Graben (Central China). Journal of Earth Science, 28(3), 545–554. doi: 10.1007/s12583-017-0900-z.

Reznichenko NV, Andrews GR, Geater RE, Strom A. 2017. Multiple origins of large hummock deposits in Alai valley, northern Pamir: implications for palaeoclimate reconstructions. Geomorphology, 285, 347–362. doi: 10.1016/j.geomorph.2017.02.019.

Roback K, Clark MK, West AJ, Zekkos D, Li G, Gallen SF, Chamlagain D, Godt JW. 2018. The size, distribution, and mobility of landslides caused by the 2015 Mw7.8 Gorkha earthquake, Nepal. Geomorphology, 301, 121–138. doi: 10.1016/j.geomorph.2017.01.030.

Robinson AC, Yin A, Manning CE, Harrison TM, Zhang S-H, Wang X-F. 2004. Tectonic evolution of the northeastern Pamir: constraints from the northern portion of the Cenozoic Kongur Shan extensional system, western China. Geological Society of America Bulletin, 116(7), 953–973. doi: 10.1130/b25375.1.

Robinson AC, Yin A, Manning CE, Harrison TM, Zhang SH, Wang XF. 2007. Cenozoic evolution of the eastern Pamir: implications for strain-accommodation mechanisms at the western end of the Himalayan-Tibetan orogen. Geological Society of America Bulletin, 119(7-8), 882–896. doi: 10.1130/b25981.1.

Robinson TR, Davies TRH, Reznichenko NV, De Pascale GP. 2015. The extremely long-runout Komansu rock avalanche in the Trans Alai range, Pamir mountains, southern Kyrgyzstan. Landslides, 12(3), 523–535. doi: 10.1007/s10346-014-0492-y.

Sato HP, Harp EL. 2009. Interpretation of earthquake-induced landslides triggered by the 12 May 2008, M7.9 Wenchuan earthquake in the Beichuan area, Sichuan Province, China using satellite imagery and Google Earth. Landslides, 6(2), 153–159. doi: 10.1007/s10346-009-0147-6.

Schurr B, Ratschbacher L, Sippl C, Gloaguen R, Yuan X, Mechie J. 2014. Seismotectonics of the Pamir. Tectonics, 33(8), 1501–1518. doi: 10.1002/2014tc003576.

Seong YB, Owen LA, Yi C, Finkel RC, Schoenbohm L. 2009. Geomorphology of anomalously high glaciated mountains at the northwestern end of Tibet: Muztag Ata and Kongur Shan. Geomorphology, 103(2), 227–250. doi: 10.1016/j.geomorph.2008.04.025.

Shao X, Ma S, Xu C, Shen L, Lu Y. 2020. Inventory, distribution and geometric characteristics of landslides in Baoshan city, Yunnan Province, China. Sustainability, 12(6), 2433. doi: 10.3390/su12062433.

Shao X, Ma S, Xu C, Zhang P, Wen B, Tian Y, Zhou Q, Cui Y. 2019. Planet image-based inventorying and machine learning-based susceptibility mapping for the landslides triggered by the 2018 Mw6.6 Tomakomai, Japan earthquake. Remote Sensing, 11(8), 978. doi: 10.3390/rs11080978.

Shao X, Xu C, Wang P, Li L, He X, Chen Z, Huang Y, Xu X. 2022. Two public inventories of landslides induced by the 10 June 2022 Maerkang Earthquake swarm, China and ancient landslides in the affected area. Natural Hazards Research, 2(4), 269–272. doi: 10.1016/j.nhres.2022.09.001.

Shi A, Wang Y, Cheng Q, Lin Q, Li T, Wünnemann B. 2023. The largest rock avalanche in China at Iymek, eastern Pamir, and its spectacular emplacement landscape. Geomorphology, 421, 108521. doi: 10.1016/j.geomorph.2022.108521.

Strom A, Abdrakhmatov K. 2018. Rockslides and rock avalanches of central Asia: Distribution, morphology, and internal structure. Elsevier, 51–90. doi: 10.1016/C2014-0-02190-9.

Tian Y, Xu C, Chen J, Zhou Q, Shen L. 2017. Geometrical characteristics of earthquake-induced landslides and correlations with control factors: a case study of the 2013 Minxian, Gansu, China, Mw 5.9 event. Landslides, 14, 1915–1927. doi: 10.1007/s10346-017-0835-6.

Tian Y, Owen LA, Xu C, Shen L, Zhou Q, Figueiredo PM. 2020. Geomorphometry and Statistical Analyses of Landslides Triggered by the 2015 M w 7.8 Gorkha Earthquake and the Mw 7.3 Aftershock, Nepal. Frontiers in Earth Science, 8, 572449. doi: 10.3389/feart.2020.572449.

Wang J. 2020. The geomorphological characteristics and kinematic mechanism of Tagarma rock avalanche. Chengdu, Southwest Jiaotong University, Master thesis, 1–103 (in Chinese).

Wang P. 2020. Research on main engineering geology problems of Xinjiang-Tibet railway. Railway Standard Design, 64(4), 7–11, 17 (in Chinese).

Wang W, Huang Y, Xu C, Li L. 2021. Development and distribution of ancient landslides in the northwest corner of the Tibetan Plateau. IOP Conference Series:Earth and Environmental Science, 861(5), 052034. doi: 10.1088/1755-1315/861/5/052034.

Wang Y, Cheng Q, Yuan Y, Wang J, Qiu Y, Yin B, Shi A, Guo Z. 2020. Emplacement mechanisms of the Tagarma rock avalanche on the Pamir-western Himalayan syntaxis of the Tibetan Plateau, China. Landslides, 17(3), 527–542. doi: 10.1007/s10346-019-01298-1.

Wang Y, Cheng Q, Lin Q, Anwen S. 2021. Observations on the sedimentary structure of prehistoric rock avalanches on the Tibetan Plateau, China. Earth Science Frontiers, 28(2), 106–124 (in Chinese). doi: 10.13745/j.esf.sf.2020.9.12.

Wang Y, Cheng Q, Shi A, Yuan Y, Qiu Y, Yin B. 2019. Characteristics and transport mechanism of the Nyixoi Chongco rock avalanche on the Tibetan Plateau, China. Geomorphology, 343, 92–105. doi: 10.1016/j.geomorph.2019.07.002.

Wang Y, Dong J, Cheng Q. 2017. Velocity-dependent frictional weakening of large rock avalanche basal facies: implications for rock avalanche hypermobility? Journal of Geophysical Research: Solid Earth, 122(3), 1648–1676. doi: 10.1002/2016jb013624.

Wang Y, Dong J, Cheng Q. 2018. Normal stress-dependent frictional weakening of large rock avalanche basal facies: implications for the rock avalanche volume effect. Journal of Geophysical Research:Solid Earth, 123(4), 3270–3282. doi: 10.1002/2018jb015602.

Xu C. 2015. Preparation of earthquake-triggered landslide inventory maps using remote sensing and GIS technologies: principles and case studies. Geoscience Frontiers, 6(6), 825–836. doi: 10.1016/j.gsf.2014.03.004.

Xu C, Dai F, Xu X, Lee YH. 2012a. GIS-based support vector machine modeling of earthquake-triggered landslide susceptibility in the Jianjiang River watershed, China. Geomorphology, 145–146, 70–80. doi: 10.1016/j.geomorph.2011.12.040.

Xu C, Xu X, Dai F, Saraf AK. 2012b. Comparison of different models for susceptibility mapping of earthquake triggered landslides related with the 2008 Wenchuan earthquake in China. Computers and Geosciences, 46, 317–329. doi: 10.1016/j.cageo.2012.01.002.

Xu C, Xu X, Shyu JBH, Gao M, Tan X, Ran Y, Zheng W. 2015. Landslides triggered by the 20 April 2013 Lushan, China, Mw 6.6 earthquake from field investigations and preliminary analyses. Landslides, 12(2), 365–385. doi: 10.1007/s10346-014-0546-1.

Xu C, Shen L, Wang G. 2016. Soft computing in assessment of earthquake-triggered landslide susceptibility. Environmental Earth Sciences, 75(9), 767. doi: 10.1007/s12665-016-5576-7.

Xu C, Xu X, Yao X, Dai F. 2014a. Three (nearly) complete inventories of landslides triggered by the May 12, 2008 Wenchuan Mw 7.9

earthquake of China and their spatial distribution statistical analysis. Landslides, 11(3), 441–461. doi: 10.1007/s10346-013-0404-6.

Xu C, Xu X, Shyu JBH, Zheng W, Min W. 2014b. Landslides triggered by the 22 July 2013 Minxian–Zhangxian, China, Mw 5.9 earthquake: inventory compiling and spatial distribution analysis. Journal of Asian Earth Sciences, 92, 125–142. doi: 10.1016/j.jseaes.2014.06.014.

Xu C, Cui Y, Xu X, Bao P, Fu G, Jiang W. 2019. An anthropogenic landslide dammed the Songmai River, a tributary of the Jinsha River in Southwestern China. Natural Hazards, 99(1), 599–608. doi: 10.1007/s11069-019-03740-y.

Xu Y, Allen MB, Zhang W, Li W, He H. 2020. Landslide characteristics in the Loess Plateau, northern China. Geomorphology, 359, 107150. doi: 10.1016/j.geomorph.2020.107150.

Xu Y, Liu Z, Allen MB, Du P, Zhang W, Li W, Tian Q. 2022. Understanding historical earthquakes by mapping coseismic landslides in the Loess Plateau, northwest China. Earth Surface Processes and Landforms, 47(9), 2266–2282. doi: 10.1002/esp.5375.

Yin Z, Wei G, Qin X, Li W, Zhao W. 2021. Research progress on landslides and dammed lakes in the upper reaches of the Yellow River, northeastern Tibetan Plateau. Earth Science Frontiers, 28(2), 46–57. doi: 10.13745/j.esf.sf.2020.9.4.

Yuan Z. 2012. Nature and timing of large landslides within an active orogeny, NE Pamir, China. Beijing, Institute of Geology, China Earthquake Administration, Master thesis, 1–67 (in Chinese).

Yuan Z, Chen J, Owen LA, Hedrick KA, Caffee MW, Li W, Schoenbohm LM, Robinson AC. 2013. Nature and timing of large landslides within an active orogen, eastern Pamir, China. Geomorphology, 182, 49–65. doi: 10.1016/j.geomorph.2012.10.028.

Zhang X, Lei L, Xu C. 2022. Large-scale landslide inventory and their mobility in Lvliang City, Shanxi Province, China. Natural Hazards Research, 2(2), 111–120. doi: 10.1016/j.nhres.2022.05.002.

Zhang Y, Wu R, Guo C, Wang L, Yao X, Yang Z. 2018. Research progress and prospect on reactivation of ancient landslides. Advances in Earth Science, 33(7), 728–740 (in Chinese). doi: 10.11867/j.issn.1001-8166.2018.07.0728.

Zhao B, Su L, Wang Y, Ji F, Li W, Tang C. 2021. Insights into the mobility characteristics of seismic earthflows related to the Palu and eastern Iburi earthquakes. Geomorphology, 391, 107886. doi: 10.1016/j.geomorph.2021.107886.

Zhao B, Wang Y, Chen M, Luo Y, Liang R, Li J. 2019. Typical characteristics of large-scale landslides in the transition belt between the Qinghai-Tibet Plateau and the Loess Plateau. Arabian Journal of Geosciences, 12(15), 470. doi: 10.1007/s12517-019-4612-9.

Zhao B, Su L, Xu Q, Li W, Xu C, Wang Y. 2023. A review of recent earthquake-induced landslides on the Tibetan Plateau. Earth-Science Reviews, 244, 104534. doi: 10.1016/j.earscirev.2023.104534.

Zheng S, Zang L, Duan S. 2018. A study on the characteristics and distribution of debris flow landslides in the mountainous areas of Qinghai-Tibet plateau. China's Manganese Industry, 36(4), 181–183 (in Chinese). doi: 10.14101/j.cnki.issn.1002-4336.2018.04.045.

Zhu Y, Dai F, Yao X, Tu X, Shi X. 2019. Field investigation and numerical simulation of the seismic triggering mechanism of the Tahman landslide in eastern Pamir, northwest China. Bulletin of Engineering Geology and the Environment, 78(8), 5795–5809. doi: 10.1007/s10064-019-01541-y.

Zhuang J, Ma P, Zhan J, Zhu Y, Kong J, Zhu X, Leng Y, Peng J. 2022. Empirical relationships of the landslides in the Chinese Loess Plateau and affect factors analysis. Geomatics, Natural Hazards and Risk, 13(1), 250–266. doi: 10.1080/19475705.2021.2020174.